

# Thermal Infrared Spectral Band Detection Limits for Unidentified Surface Materials

Laurel E. Kirkland<sup>1</sup>, Kenneth C. Herr<sup>2</sup>, and John W. Salisbury<sup>3</sup>

**Abstract.** Infrared emission spectra recorded by airborne or satellite spectrometers can be searched for spectral features to determine the composition of rocks on planetary surfaces. Surface materials are identified using detections of characteristic spectral bands. Here we show how to define whether to accept an observed spectral feature as a detection when the target material is unknown. We also use remotely sensed spectra measured by TES and SEBASS to illustrate the importance of instrument parameters and surface properties on band detection limits, and how the variation in signal-to-noise ratio with wavelength affects which bands are most detectable for a given instrument. The spectrometer's sampling interval, spectral resolution, signal-to-noise ratio as a function of wavelength, and the sample's surface properties influence whether the instrument can detect a spectral feature exhibited by a material. As an example, in the 6–13  $\mu\text{m}$  wavelength region, massive carbonates exhibit two bands: a very strong, broad feature at  $\sim 6.5 \mu\text{m}$ , and a less intense, sharper band at  $\sim 11.25 \mu\text{m}$ . Although the  $6.5 \mu\text{m}$  band is stronger and broader in laboratory measured spectra, the  $11.25 \mu\text{m}$  band will cause a more detectable feature in TES spectra.

## 1. Introduction

Remote sensing by airborne and satellite spectrometers is currently being used to detect minerals and rocks on the Earth and planetary surfaces. To identify the minerals present, the remotely sensed spectra may be searched for matches to signatures of materials using analog laboratory spectra. However, hundreds of minerals are possible, and the signatures vary non-linearly with grain size, which gives a wide continuum of signatures. Thus the range of signatures to search for is commonly constrained using ground truth or general geologic knowledge. The fewer the channels that are measured by the remote sensing instrument, the more important it becomes to constrain the possible mineral signatures present. If a remotely sensed spectrum shows no evidence of a band that is known to exist in a material, then this may be used to place upper limits on the amount of the material present.

Several remote sensing studies of solid materials

examined detection limits based on spectral signature mapping, such as linear spectral mixing models of the full spectrum using laboratory spectra,<sup>1,2,3</sup> or optimal matched filters.<sup>4,5,6</sup> Spectral signature mapping techniques have in common the same first step, which is to define the spectral signatures to search for using a spectral library or from within the scene. The successful application of these methods to identifying mineral signatures in remotely sensed spectra is affected in main by two issues.

First is how well the remotely sensed spectra can be calibrated to a unit such as reflectance or apparent emissivity for comparison to laboratory spectral endmembers. Instrument calibration and atmospheric compensation uncertainties, and variations in the background continuum also increase the difficulty of making a direct match to laboratory spectra. The situation is made more difficult when there are no accompanying ground truth measurements to use to define signatures to search for in the remotely sensed spectral data base.

Second, since the spectral shape varies with particle size, weathering, and surface properties that are unrelated to composition, the quality of the result depends on how inclusively the chosen endmembers represent the variations present in the data set, and whether the remotely sensed spectra have the spectral resolution, range, and SNR to discriminate between all the end-

---

L. Kirkland is with the Lunar and Planetary Institute, Houston, Texas, 77058, email [kirkland@lpi.usra.edu](mailto:kirkland@lpi.usra.edu). K. Herr is with The Aerospace Corporation, Los Angeles, California, 90009. J. Salisbury is retired from Johns Hopkins University, Palm Coast, Florida 32137.

Received 10 October 2000; revised manuscript received 3 April 2001.

members. The possible presence of non-linear mixing effects, such as occurs for very small particle sizes,<sup>6,7,8,9,10</sup> significantly increases the difficulty of formulating an appropriate range of endmember signatures to use to search the spectral data base.<sup>5,6</sup> Searching for the spectral signature matches requires the desired spectral signatures to be pre-defined, although the signatures may not be well known when there is no accompanying ground truth. Thus these powerful techniques are most optimal when there is knowledge about the range of materials present.

Other studies have focused on discriminating materials using statistical variations within the data set<sup>11,12,13</sup> or unidentified endmembers defined from within the data set.<sup>14,15</sup> These approaches may discriminate between spectral classes, but when the signatures cannot be directly compared to laboratory spectra, the classes must be identified using ground truth.<sup>16</sup> Gases are commonly detected against the background signature in relatively narrow gas bands.<sup>17,18,19</sup>

Thus while spectral signature mapping methods such as linear mixture modeling and optimal matched filters are very powerful, remote sensing studies that have to proceed without benefit of ground truth must also include analysis of the spectral data base from a different perspective. If the target material composition is unknown and cannot be well-constrained, for example as occurs in remote sensing measurements of Mars and some terrestrial studies that lack ground truth, then the signatures to search for are unknown. In addition, the available spectral libraries may not contain spectra of all the possible materials and particle sizes present. This is especially a consideration when weathering products are present because the composition, texture, particle size, and spectral signatures of weathering products vary considerably. As a result, remotely sensed spectra of unconstrained targets are also searched for detections of spectral features without assuming an *a priori* signature, and then attempts are made to identify the observed features. If a feature is detected that does not match those present in the available spectral libraries, then the shape and center of the observed feature is used to constrain which additional materials to examine in the laboratory to search for a spectral match to identify the unknown signature.

The minimum amount of a material that can be detected depends in part on the spectral band strength (spectral contrast) that the material exhibits at the spectral resolution and sampling of the instrument, the amount of material present, and the signal-to-noise ratio (SNR) of the recorded spectrum.

For example, in the 6–13  $\mu\text{m}$  wavelength region, there are two clear carbonate bands: a very strong, broad feature at  $\sim 6.5 \mu\text{m}$ , and a weaker, sharper band at  $\sim 11.25 \mu\text{m}$ . However, while the  $6.5 \mu\text{m}$  band is stronger and broader, it will not necessarily be more detectable

than the  $11.25 \mu\text{m}$  band by a given remote sensing instrument, since the instrument performance as a function of wavelength and the surface properties of the sample studied impact the detection limit. Noise limits the minimum band depth that can be detected, and since signal varies with wavelength, the SNR and detection limit also vary with wavelength. Spectral resolution also affects the detection limit. Poorer spectral resolution causes the band recorded to be shallower and broader, lowering the apparent spectral contrast. As a result an instrument that measures with poorer spectral resolution must measure with higher SNR in order to detect a material with the same sensitivity.

Another important effect is the variation in band contrast with material properties that are unrelated to composition. The spectral contrast of strong bands (called reststrahlen bands) decreases with increasing surface roughness or decreasing particle size. Thus spectral band depth is not a function of composition alone, but also of physical properties. However, published detection limits often do not state the background assumptions about the target's physical properties, such as grain size and surface roughness. For clarity, the surface properties and particle sizes should always be included when stating a detection limit.

If a spectrum measured of an unknown surface exhibits a possible spectral feature, we would like a quantified method to determine whether to accept the feature as a detection. However, in remote sensing compositional studies of solid surfaces, there is no clearly established method to calculate the minimum band depth a single feature of unknown origin must exhibit in a remotely sensed spectrum to be accepted with a set confidence level. For a case in point, Figure 1 shows an example remotely sensed spectrum measured of Mars by the 1996 Global Surveyor Thermal Emission Spectrometer (TES, 6–50  $\mu\text{m}$ ).<sup>20</sup> The spectrum has been converted to apparent emissivity by division of the Planck blackbody curve at the estimated surface temperature. In studies of Mars, the surface kinetic temperature is commonly estimated as the brightness temperature in the  $\sim 7.8 \mu\text{m}$  region,<sup>21,22,23</sup> and for this example we use the brightness temperature at  $1290 \text{ cm}^{-1}$  ( $7.75 \mu\text{m}$ ), which is 270 K. Noise causes the emissivity in Figure 1 to exceed 1.0 at shorter wavelengths. We desire to determine whether any given feature in the spectrum may be accepted with a set confidence level as a detection relative to the local continuum.

Here we present a method to quantify this minimum depth, the band detection limit. A well-defined method will facilitate discussions of detection limits, and determinations of which features to accept as a detection. The band detection limit depends on the SNR of the spectrum, the band width at the spectral resolution and spectral sampling interval of the instrument, and the desired confidence level.

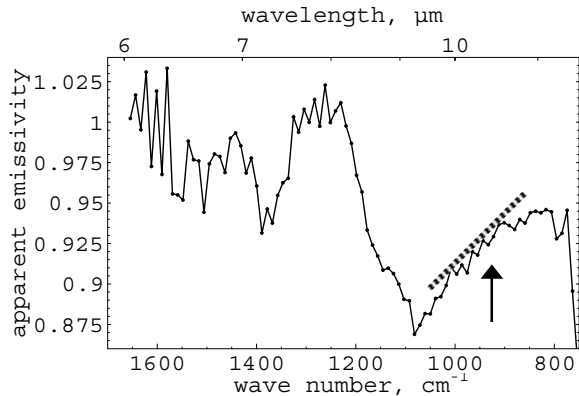


Fig. 1: Example spectral feature. This shows a typical TES spectrum measured of Mars. Transmission through the silicate aerosol dust is the main contributor to the broad, strong  $\sim 1100 \text{ cm}^{-1}$  band. The dashed line illustrates the approximate local continuum in the  $\sim 925 \text{ cm}^{-1}$  region. We desire to quantify which spectral features to accept as a detection with a desired confidence level relative to the noise and local continuum. For example, should the feature marked with the arrow at  $\sim 925 \text{ cm}^{-1}$  be accepted as a detection? TES spectrum 57023856, from the NASA archive of TES data.

We will also illustrate the variation in the detection limit as a function of instrument and target characteristics, and show the importance of including these characteristics with any statement of detection limits. To provide examples of remotely sensed thermal infrared spectra, we utilize spectra from TES and the airborne hyperspectral Spatially Enhanced Broadband Array Spectrograph System (SEBASS,  $7.57\text{--}13.52 \text{ }\mu\text{m}$ ), and for an example laboratory signature, we utilize calcite. We will focus on the calcite bands near  $6.5$  and  $11.25 \text{ }\mu\text{m}$  to provide examples of (1) stronger and weaker spectral features; (2) narrow and wide spectral features; and (3) a range in Planck blackbody signal,<sup>24</sup> and thus SNR. This combination allows the best illustration of the variation of the detection limit with wavelength, band width, and SNR. However, the method described can be applied to any remotely measured data set or infrared wavelength region.

## 2. Causes of Variations in Band Depth

Material properties that are unrelated to composition cause variations in spectral band strengths, so a statement of detection limits should carry with it a description of the material's spectral and physical properties, and not just the composition. The most important surface properties are roughness effects that cause a cavity (hohlraum) effect, and particle size and roughness on a scale that causes volume scattering.

### 2.1. Cavity Effect

The primary effect of increasing surface roughness at

all scales is the increasing cavity (hohlraum) effect. The cavity effect occurs when energy emitted from a cavity undergoes multiple scattering from internal cavity surfaces, which reduces spectral contrast by increasing the total emissivity.<sup>25,26,27</sup> The effective emissivity increases nonlinearly with the number of times the energy is reflected before exiting the cavity (Figure 2), and is given by:<sup>27</sup>

$$\epsilon_e = 1 - (1 - \epsilon)^{(count+1)} \quad (1)$$

where  $\epsilon_e$  = the effective emissivity;  $\epsilon$  = the true emissivity of the cavity wall; and *count* = the number of times the energy is reflected.

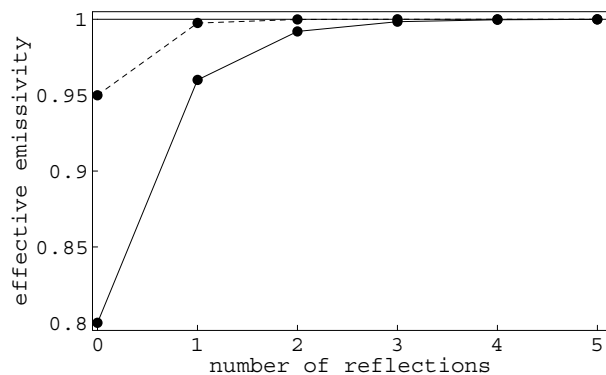


Fig. 2: Cavity effect. The effective emissivity increases with the average number of reflections of the exiting radiance. This plot illustrates the increase in effective emissivity with number of reflections, assuming an absolute emissivity of 0.8 (solid line) or 0.95 (dashed line), using Equation 1. A variety of common effects may cause cavities, such as pits that occur between individual rocks in a pile of pebbles or boulders; grooves or joints in rocks or outcrops; weathering facets or pits cut into individual rocks, and vesicles that are part of the rock texture.

In general, the greater the ratio of the cavity depth to entrance width, the greater the number of reflections and increase in total emissivity, and the lower the observed spectral band contrast for all the bands in the spectrum.<sup>26</sup> Therefore lower spectral band contrast is a direct result of the presence of pits or vesicles in the target material. Cavities may occur at a variety of scales, such as pits that occur between individual rocks in a pile of pebbles or boulders; grooves or joints in rocks or outcrops; and weathering facets or pits cut into individual rocks. In addition, when a mineral is pulverized, it loses spectral contrast relative to a polished surface because of the resulting interstices between grains form cavities that reduce spectral contrast in the same way as cavities that occur in a pile of pebbles or boulders.

## 2.2. Volume Scattering

Volume scattering occurs when the optical depth of a particle decreases enough for photons to survive passage through the volume of a grain.<sup>6,7,8,9,10</sup> This may occur in a small particle, or from the presence of optically thin edges of larger particles, and microscopically rough surfaces.

As previously noted, when a mineral is pulverized, it loses spectral contrast compared to a polished surface due to the cavity effect. As the particles become even smaller, they also become optically thin, and then volume scattering also subtracts from the spectral contrast of the reststrahlen bands. When the scale of the surface roughness is fine enough, this creates many optically thin, rough edges, and multiple scattering becomes in part volume scattering. This can be discerned when the shape of the reststrahlen band is changed by self-absorption, and shifts from having the character of a spectrum measured in reflectance or emission toward a spectrum measured in transmission.<sup>10</sup> The effect is non-linear,<sup>7,8,9</sup> and in field spectra increases the difficulty of accurate spectral signature mapping.<sup>5,6</sup>

## 3. Remote Sensing Data Used

We focus on TES spectra to illustrate the variation in detection limits with instrument parameters. We also include a brief description of airborne, terrestrial SE-BASS spectra, which we use to provide an additional example of effects present in field measurements vs. laboratory spectra.

### 3.1. TES

At the heart of TES is a Michelson interferometer spectrometer that measures from  $\sim 6\text{--}50\ \mu\text{m}$  ( $1667$  to  $200\ \text{cm}^{-1}$ ).<sup>20</sup> In the most commonly used spectral mode, the "10  $\text{cm}^{-1}$  sampling mode," TES returns spectra containing 143 discrete measurements over a range of  $\sim 1470\ \text{cm}^{-1}$ , and records one measurement every  $10.58\ \text{cm}^{-1}$ . In this mode, TES has a mirror throw of  $0.25\ \text{mm}$ ,<sup>20</sup> which gives an unapodized spectral resolution of  $20\ \text{cm}^{-1}$  if defined as the first zero crossing of the unapodized sinc response function<sup>28</sup>, or  $12.1\ \text{cm}^{-1}$  if measured as the full width at half maximum of the sinc response function.<sup>20</sup> TES also has a "5  $\text{cm}^{-1}$  sampling mode," which has better spectral resolution and records 286 measurements per spectrum, but these spectra were only occasionally taken during the period for which data are currently available, and are not used here.

TES has 6 detectors in a  $2 \times 3$  array, and each detector is mounted off the optical axis. Optical apodization caused by the off-axis positioning of each detector within the array has three effects, which are to (1) degrade the spectral resolution from the value obtained using only the mirror throw; (2) cause the spectral resolution to vary with wavelength; and (3) cause each detector to measure a slightly different wave-

length.<sup>20,28</sup> The two center detectors (2 and 5) are closest to on-axis,<sup>29</sup> and thus have the best spectral resolution (Figure 3). To provide consistent spectral resolution and wavelength measurements for this study, we used detector 5, which measures with the best spectral resolution.

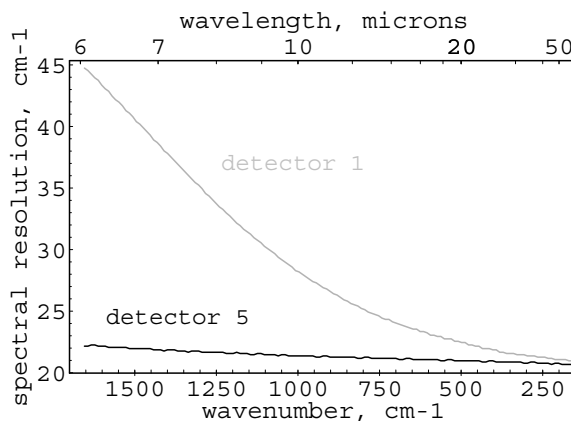


Fig. 3: TES spectral resolution. This shows the TES spectral resolution as modeled by the TES team. The gray (upper) curve shows the values for detector 1, which has the poorest spectral resolution of the 6 detectors, and the black (lower) curve for detector 5, which has the best spectral resolution. Optical apodization<sup>28</sup> from the off-axis positioning of the detectors causes the difference.<sup>20</sup> The nominal TES spectral resolution is  $20\ \text{cm}^{-1}$ . The data shown are from the NASA Planetary Data System (PDS) archive of TES data, modified from their presentation as the full width at half maximum of the sinc function to the more standard sinc first zero crossing,<sup>28</sup> using a scale factor of  $20/12.1\ \text{cm}^{-1}$ .

The digitization noise for TES varies with the maximum signal measured. TES measures interferograms in volts, and calculates the Fast Fourier Transform (FFT) of the interferograms onboard. Only these transformed spectra are returned to Earth, in uncalibrated units called "transformed volts".<sup>29</sup> Before being relayed to Earth, spectra are digitized to 11 bits plus sign, and each spectrum has a scaling factor applied, using:

$$f_{ch} = (raw_{ch}) \cdot 2^{scale} \quad (2)$$

where  $f_{ch}$  is the formatted data in transformed volts that is transmitted to Earth;  $ch$  is the channel, and TES has 143 channels per spectrum;  $raw$  is the unscaled, 12-bit value; and  $scale$  is a single exponent value that is assigned onboard to all the channels in a given spectrum.<sup>30</sup> TES selects the scale value based on the maximum absolute value recorded in the interferogram. Deep space spectra typically have a scale of 7 because they record a large maximum absolute value due to the large difference in temperature between the instrument

and deep space. The internal blackbody spectra typically have a scale of 2 or 3, and typical daytime, non-polar spectra of Mars have a scale of 6.

The full 11 bits possible are spread over the chosen scaled range, so that the TES digitization precision varies with the scale assigned. For example, a scale of 7 has digitization steps of 0.0625 transformed volts; a scale of 6 and 5 have digitization steps of 0.03125 and 0.015625 transformed volts, etc. Thus for TES the digitization noise varies with the maximum signal measured, so that spectra with a smaller assigned scale have lower digitization noise. Deep space and limb spectra have the highest digitization noise, and internal blackbody spectra the lowest.

### 3.2. SEBASS

The airborne hyperspectral Spatially Enhanced Broadband Array Spectrograph System (SEBASS) is a cooled prism spectrometer. It measures in the mid- and long-wave infrared terrestrial transmission "windows" comprising two wavelength ranges: 4132–1876  $\text{cm}^{-1}$  (2.42–5.33  $\mu\text{m}$ ) and 1321–740  $\text{cm}^{-1}$  (7.57–13.52  $\mu\text{m}$ ).<sup>31</sup> Each range is measured in 128 channels, with a spectral resolution of 7  $\text{cm}^{-1}$  at 890  $\text{cm}^{-1}$  (defined as two times the 3.5  $\text{cm}^{-1}$  sampling interval), and a one milliradian field of view per pixel. SEBASS operates as a pushbroom instrument, using two 128 x 128 detector arrays, and the entire optical bench is cooled to 4 K using liquid helium. It is operated by The Aerospace Corporation's Office of Spectral Applications, under the direction of John Hackwell. We utilize here the longer wavelength SEBASS data, and hyperspectral images that are 128 pixels wide and 2000 pixels long, measured with a surface spatial resolution of  $\sim 2 \times 2 \text{ m}^2$ .

### 4. Method

The band detection limit is the minimum percent band depth that a feature of unknown origin in a single spectrum must have to be accepted as a detection with the desired confidence relative to the noise. It depends on the (1) instrument SNR, (2) instrument spectral resolution and sampling interval, (3) target spectral band depth, (4) band width, and (5) desired signal level above the noise. Below we detail how to calculate each of the parameters listed above, and then explain how they are combined to calculate the desired detection limit, and we discuss atmospheric effects that degrade the detection limit.

#### 4.1. SNR

To calculate the SNR, the signal at a given temperature and the noise must be determined, and then ratioed. The standard signal is typically calculated for a 300K blackbody target for terrestrial measurements, and a 270K target for Mars.

For TES, we calculate the 270K signal using spectra

recorded of the TES internal blackbody calibration target, using raw units, which for TES are called "transformed volts." The calculation works similarly using any raw unit; for example, we use Digital Numbers (DN) in our calculations for spectra from the 1969 Mariner Mars Infrared Spectrometer (IRS).

To calculate the signal, first we assume that deep space is at 0K. Next we make a linear fit for each TES channel from an average deep space spectrum to a calibration blackbody target spectrum (Figure 4). The blackbody spectrum shown in Figure 4 was recorded by TES in-flight of its internal blackbody target at 286.6K. Negative values represent measurements taken of a target colder than the TES internal signature, and positive values a target warmer than TES.<sup>32</sup> A linear interpolation to 270K is made using a two point fit to:

$$\begin{aligned} x_1, y_1 &= \text{Rad}_{0\text{K}}, \text{DS}_{\text{volts}}[\lambda] \\ x_2, y_2 &= \text{Rad}_{286.6\text{K}}, \text{BB}_{\text{volts}}[\lambda], \end{aligned} \quad (3)$$

where  $\text{Rad}_{0\text{K}}$  and  $\text{Rad}_{286.6\text{K}}$  give the blackbody radiance at 0K and 286.6K respectively;  $\text{DS}[\lambda]$  is the deep space spectrum value in transformed volts for each wavelength measured, and  $\text{BB}[\lambda]$  is the blackbody target. The fit is then solved for each wavelength measured at  $x = \text{radiance at 270K}$ , which gives the values for the desired standard temperature. Finally, the signal is the difference between the 270K curve and the deep space curve (Figure 4).

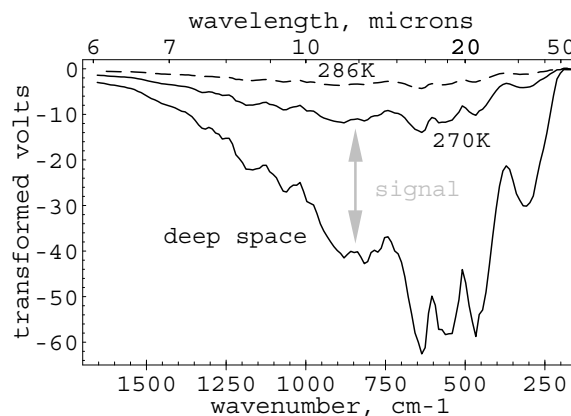


Fig. 4: TES signal. The upper, dashed line shows an average of 3 spectra of the internal blackbody target at a temperature of 286.6K, and the bottom trace shows an average of 5 deep space spectra. The middle trace shows the blackbody spectrum interpolated to a 270K target. For the signal-to-noise ratio calculation, the *signal* at a given wavenumber is the difference between the 270K and DS curves. This plot shows that TES has the highest signal in the  $\sim 1000$  to  $350 \text{ cm}^{-1}$  region. Blackbody target measurements are spectra 576023692 to 96, and the deep space measurements are spectra 575978746 to 54.

We calculate the noise using deep space spectra, based on the assumption that at a given wavelength, noise causes all the variation in sequential measurements of deep space. TES periodically measures three or five deep space spectra sequentially for its calibration. The TES *root mean square (rms) noise* is calculated by first calculating the variance at each wavelength, using the raw, sequentially measured deep space spectra. Then the rms noise is the average of the square root of the variance from all wavelengths. For the example shown here, the *peak-to-peak noise* is calculated from five deep space spectra by first calculating the difference between the maximum and the minimum signal value measured at all 143 wavelengths (Figure 5). Then the peak-to-peak noise is the maximum difference. Finally, the signal-to-noise ratio is the signal at each wavelength measured divided by either the rms or peak-to-peak noise (Figure 6).

Since we desire to examine the detection limit for individual spectra, we use the peak-to-peak noise rather than the rms noise. Peak-to-peak noise is typically  $\sim 5$  times the rms noise,<sup>28</sup> and for the TES spectra examined, the factor is 5.2. It is also common to use averages of spectra or other processing techniques to increase the SNR. When this is done, the SNR should be re-calculated to account for the improvement.

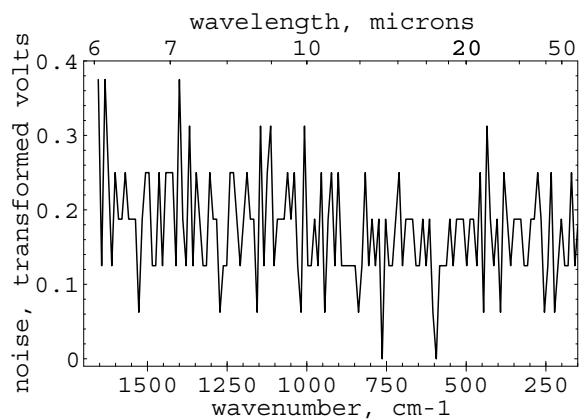


Fig. 5: TES noise. This shows the difference between the maximum and minimum value measured at each wavelength of 5 TES deep space spectra (spectra 575978746 to 54). For the signal-to-noise ratio calculation, the *peak-to-peak noise* is the maximum of the 143 values shown, which here is 0.375 transformed volts. The "stepped" appearance of the plot reflects the digitization noise, and the digitization steps are 0.0625 transformed volts for deep space spectra, which translates to a peak-to-peak noise of 6 digitization steps. This indicates digitization noise does not dominate the peak-to-peak noise present in TES spectra.

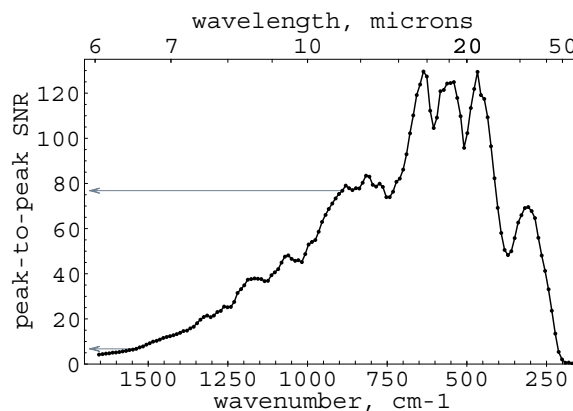


Fig. 6: SNR vs. wavelength. Shown are the peak-to-peak signal-to-noise ratio values for TES when measuring a black-body at 270K. Higher values represent higher quality. Detector response and the Planck radiance signal cause the broad shape of the curve, while instrument absorptions cause the finer detail. For reference, arrows are drawn to indicate the SNR values at 891 and 1538  $\text{cm}^{-1}$  (11.2 and 6.5  $\mu\text{m}$ ), near two of the carbonate band centers examined.

#### 4.2. Spectral resolution and sampling

The band area recorded in a spectrum is essentially invariant with the instrument's spectral resolution, but the measured band becomes wider and shallower as spectral resolution degrades.<sup>33</sup> We use hemispherical reflectance laboratory spectra measured by Paul Adams (The Aerospace Corporation) at a resolution of 4  $\text{cm}^{-1}$ , which is sufficient to record accurately the full depth of the mineral features of interest. To simulate the signature that the remote sensing instrument would record, we convolve each laboratory spectrum to the nominal spectral resolution of the instrument (20  $\text{cm}^{-1}$  for TES), and sample the resulting spectra at the same band centers as measured by TES.

We examined laboratory spectra measured of a limestone and a calcrete sample from the Mormon Mesa, Nevada<sup>34,35</sup> (Figure 7). These spectra were measured in hemispherical reflectance and converted to emissivity using Kirchoff's Law,<sup>36</sup> and had the continuum removed by division to cubic spline fits.<sup>37</sup> X-ray diffraction shows that the limestone consists mainly of calcite, and the calcrete mainly of calcite and quartz. Analysis using acid dissolution indicates the limestone is composed of 99.5% calcite, and the calcrete 92% calcite.<sup>38</sup> Since we would like to compare band depths for pure endmembers, the calcrete sample has been scaled to the spectral contrast it would exhibit for the 890 and 1540  $\text{cm}^{-1}$  bands if it consisted entirely of calcite, using scaled emissivity = (measured emissivity-0.08)/0.92. The cavity effect caused by the rough, pitted surface, and volume scattering from the small, angular grains cause the lower band contrast exhibited by the calcrete relative to the limestone.<sup>34</sup>

### 4.3. Mineral band depth

We utilize the laboratory spectra from step 2 to calculate the mineral band depths, expressed in percent. The depth of narrow bands, such as the 11.25  $\mu\text{m}$  calcite band, is most strongly affected by lower spectral resolution and more sparse sampling that are typical of most remotely sensed spectra relative to laboratory spectra. Both make the recorded feature have lower spectral contrast.

### 4.4. Mineral band width

The band width is measured as the full width at the half maximum of the band depth,<sup>39</sup> using the laboratory spectra from step 2 above and shown in Figure 7.

### 4.5. Confidence factor

This sets how much spectral contrast relative to the peak-to-peak noise level a feature should have to be accepted with the desired confidence. Lower values represent acceptance at closer to the noise level, and values most commonly used are 1, 2, and 3.<sup>40</sup> Here we focus on a confidence factor of 2 to illustrate results for the mid-range.

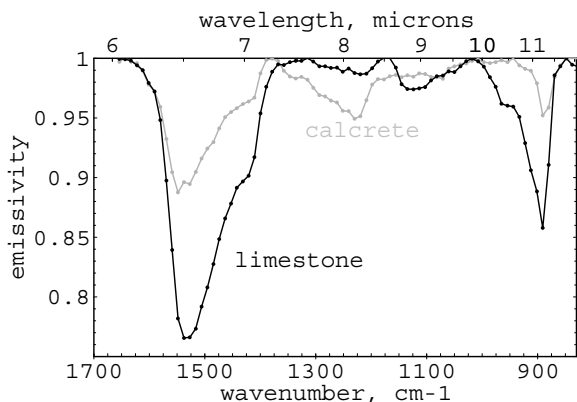


Fig. 7: Laboratory spectra. These spectra are convolved to 20  $\text{cm}^{-1}$  spectral resolution, and sampled at the same intervals as TES, and have had the continuum removed by division to cubic spline fits. Both the limestone and the calcrete consist predominantly of calcite. A pitted, rough surface causes a cavity effect, and small, angular grains cause volume scattering, both of which decrease the spectral contrast in the calcrete relative to the limestone. This shows the importance of stating the assumed band contrast for a derived detection limit for a given material, such as calcite, since band contrast varies with properties unrelated to the composition. Spectra were measured by Paul Adams (The Aerospace Corporation), converted to emissivity using one minus hemispherical reflectance.

### 4.6. Atmosphere

Atmospheric effects are very important in remote sensing surface studies, and there are many methods of

atmospheric compensations. The subject warrants long standalone discussions that are too extensive to include here, but Shott<sup>41</sup> gives an excellent review of methods, and Smith et al.<sup>42</sup> describe methods applied to TES.

Atmospheric absorptions will attenuate the signal from the surface, thus decreasing the surface signal and lowering the effective SNR. In addition, at the lower spectral resolution that is typical of many remote sensing measurements, the atmospheric signature can mimic typical mineral features, thus making it less certain whether a mineral or atmospheric component causes a given feature. The lower the spectral resolution of the instrument, the greater the loss of characteristic spectral detail, and the more difficult this problem becomes. Also, in general, the stronger the atmospheric absorption, the greater the uncertainty in the atmospherically compensated signature.

We do not include these effects in the example calculation of detection limits because they depend strongly on the particular atmospheric compensation used, the atmospheric signature, and whether accompanying ground truth is present to increase confidence in the result. However, atmospheric effects may be included in the band detection limit calculation by including uncertainties in the atmospheric compensation as a form of noise in the band detection limit calculation. Smith et al.<sup>42</sup> estimate their TES atmospheric compensation errors as 0.00232 in apparent emissivity, which is approximately one-fifth the peak-to-peak SNR.

## 5. Results

Once the data from steps 4.1–4.6 are determined, the band detection limit may be calculated and the results compared to laboratory measurements. The detection limit (DL) is calculated using:

$$DL = \frac{100 \times \text{Confidence Factor}}{\frac{\text{signal}}{\text{noise}_{\text{ptop}} / 2} \times \sqrt{\frac{\text{Band FWHM}}{\text{Sampling Interval}}}} \quad (4)$$

where  $DL$  = the minimum band depth required for detection;  $\text{Confidence Factor}$  = contrast relative to the peak-to-peak noise level a feature should exhibit to be accepted;  $\text{signal}$  = signal used in the SNR calculation;  $\text{noise}_{\text{ptop}}$  = peak-to-peak noise. The noise is divided by 2 to account for the measurement being made relative to the local continuum, so the deflection is referenced to one-half the peak-to-peak noise rather than the full peak-to-peak noise;  $\text{Band FWHM}$  = target band full width at the half maximum of the band depth; and  $\text{Sampling Interval}$  = spacing of points measured, which is 10.58  $\text{cm}^{-1}$  for TES. The square root accounts for the increase in signal-to-noise that occurs with the square root of the number of points measured on the band.

Lower numbers for the detection limit indicate lower spectral contrast is required for detection. Thus a more sensitive detection results from a higher SNR, denser wavenumber sampling interval, and a material with a wider and deeper band. The confidence factor also affects the detection limit, so that a higher confidence factor requires a greater band contrast for acceptance.

Figure 8 shows the detection limit for TES for a feature with a full width at half maximum of  $30\text{ cm}^{-1}$ , calculated using a confidence factor of 2, the TES peak-to-peak SNR shown in Figure 6, and a sampling interval of  $10.58\text{ cm}^{-1}$ . It illustrates the variation in the band detection limit with wavelength for a feature with a given width, and why spectral signature fits should be weighted by the varying SNR with wavelength.

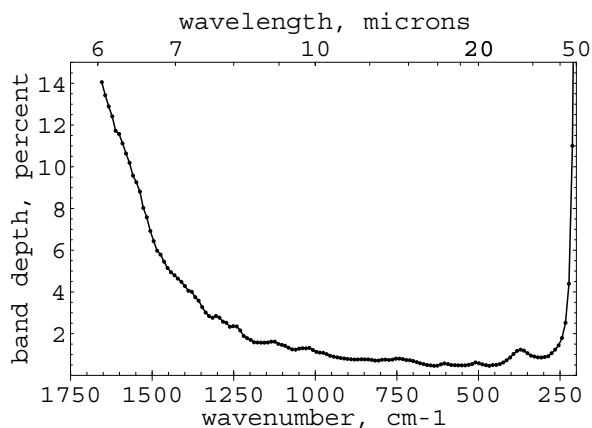


Fig. 8: Detection limit as percent band depth vs. wavenumber. This shows the results for a single TES spectrum, computed using a confidence factor of 2, a band full width at half maximum of  $30\text{ cm}^{-1}$ , and assuming a surface temperature of  $270\text{K}$ . This gives a detection limit of  $0.8\%$  at  $890\text{ cm}^{-1}$ , which is the band depth that a TES spectrum would have to exhibit at that wavenumber for the band to be accepted with the desired confidence level.

Once the detection limit is determined, then we can determine whether the instrument may detect a feature exhibited by a given material, and the percent aerial coverage required for the feature to be detected with the desired confidence. We label the percent aerial coverage required for detection the "material detection limit," to differentiate it from the band detection limit.

Table 1 gives the measured band depths and the band detection limit values for the  $1540$  and  $890\text{ cm}^{-1}$  bands exhibited by the limestone and calcrite. For TES spectra to exhibit a spectral feature that can be detected with the desired confidence, the material would have to exhibit a band depth greater than the band detection limit. For example, at  $890\text{ cm}^{-1}$  the limestone measured in the laboratory exhibits a band depth of  $14.2\%$  and

TES has a band detection limit of  $0.7\%$  with a confidence factor of 2, so TES would detect an  $890\text{ cm}^{-1}$  feature with the desired confidence factor if TES measured the material under similar conditions as those present for the laboratory measurement (the target surface is smooth at sizes larger than the sample and fills the field of view, and no atmospheric effects).

The calculated detection limits also illustrate a critical and often overlooked point about which bands are most detectable. For limestone, the ratio of the band detection limit at  $1540\text{ cm}^{-1}$  to  $890\text{ cm}^{-1}$  shows that because of the varying SNR vs. wavelength, the  $1540\text{ cm}^{-1}$  band would need to be 6.6 times deeper than the  $890\text{ cm}^{-1}$  band for it to be as detectable in TES spectra. However, the band is only 1.6 times as deep. This means that for this example instrument, the  $890\text{ cm}^{-1}$  band of this limestone is actually more detectable than the  $1540\text{ cm}^{-1}$  band, even though the  $890\text{ cm}^{-1}$  band is narrower and weaker. This important point is often overlooked, and should be considered both when searching a data set for the signature of a desired material, and when setting detection limits. A similar result is obtained for the calcrite, with the ratio in detection limit of 6.0, but a band depth ratio of only 2.3.

**Table 1: Results for two example carbonates**

|   | limestone            | calcrite             |
|---|----------------------|----------------------|
| $890\text{ cm}^{-1}$ band width                       | $40\text{ cm}^{-1}$  | $30\text{ cm}^{-1}$  |
| $890\text{ cm}^{-1}$ band depth                       | $14.2\%$             | $4.8\%$              |
| $890\text{ cm}^{-1}$ band detection limit (CF=2)      | $0.7\%$              | $0.8\%$              |
| $890\text{ cm}^{-1}$ band detection limit (CF=3)      | $1.0\%$              | $1.2\%$              |
| $1540\text{ cm}^{-1}$ band width                      | $118\text{ cm}^{-1}$ | $110\text{ cm}^{-1}$ |
| $1540\text{ cm}^{-1}$ band depth                      | $23.4\%$             | $11\%$               |
| $1540\text{ cm}^{-1}$ band detection limit (CF=2)     | $4.4\%$              | $4.6\%$              |
| $1540\text{ cm}^{-1}$ band detection limit (CF=3)     | $6.7\%$              | $6.9\%$              |
| band detection limit ratio, $1540:890\text{ cm}^{-1}$ | 6.6                  | 6.0                  |
| band depth ratio, $1540:890\text{ cm}^{-1}$           | 1.6                  | 2.3                  |

*detection limit ratio* is the ratio of the  $1540\text{ cm}^{-1}$  to the  $890\text{ cm}^{-1}$  detection limit; and *band depth ratio* is the ratio of the  $1540$  to  $890\text{ cm}^{-1}$  band depths. Detection limits calculated for a confidence factor (CF) of 2 or 3, as listed after the detection limit.

The above calculations assume the material fills the instrument's field of view. To provide a simple illustration of the effects of mixed materials in the field of view (mixed pixel effect), we assume a checkerboard mix with a blackbody, so that if there is 0% coverage by calcite, the spectrometer measures emissivity ( $\epsilon$ ) = 1, and for 100% calcite coverage, the spectrometer sees an emissivity equal to the measured calcite band depth. Then the band depth of the mixture ( $d_m$ ) is given by:

$$d_m = f \cdot d \quad (5)$$

where  $f$  is the fractional coverage by the carbonate, and  $d$  is the band depth of the pure material. Then the minimum percent coverage by the carbonate ( $f_{min}$ ) required for detection by the instrument (material detection limit) is given by:

$$f_{min} = \frac{d_m}{d} = \frac{DL}{d} \quad (6)$$

where  $DL$  is the band detection limit.

For example, for calcrete at  $890 \text{ cm}^{-1}$ , TES has a band detection limit of 0.8% with a confidence factor of two, and the calcrete exhibits a band depth of 4.8%, so TES could detect the  $890 \text{ cm}^{-1}$  feature if pure calcrete covers 16% of the surface and is measured under similar conditions as those present in the laboratory (i.e. smooth surface on a scale larger than the sample and no atmospheric interference or reflected downwelling radiance). Under these conditions, the material detection limit with a confidence factor of 2 based on the  $890 \text{ cm}^{-1}$  band is 16% for calcrete and 5% for the limestone, and using the  $1540 \text{ cm}^{-1}$  band is 42% for calcrete and 19% for limestone. It is important to note that in this case, the weaker  $890 \text{ cm}^{-1}$  band sets the more sensitive limits, not the stronger and wider  $1540 \text{ cm}^{-1}$  band.

## 6. Field vs. lab measurements

The detection limits we have presented are based on band depths measured in the laboratory, convolved to the spectral resolution and sampling interval of the example instrument. However, effects present in the field that are not reproduced in the laboratory reduce the spectral contrast, so that the contrast recorded of a material by a field instrument is commonly not as strong as that recorded in the laboratory. Effects that reduce the spectral contrast may be included by an appropriate adjustment of the material's assumed band depth ( $d$ ). In addition, measurements recorded by a satellite instrument have inherently greater instrument uncertainties than laboratory measurements, because the satellite instrument calibration cannot be rechecked under as controlled conditions as are present in the laboratory. Hanel et al.<sup>43</sup>, Beer<sup>44</sup>, and Schott<sup>45</sup> give extensive discussions of calibration effects and tradeoffs. Instrument uncertainties can be accounted for using an appropriate adjustment of the confidence factor. Christensen<sup>29</sup> gives no known calibration errors for TES that will affect the detection limit. As discussed previously, uncertainties in the atmospheric compensation also create greater uncertainties in remotely sensed spectra.

Two important effects that reduce the spectral contrast in the field are reflected downwelling radiation,<sup>46</sup> and a cavity effect that occurs from roughness on a scale larger than the laboratory sample, for example as occurs in a pile of pebbles or boulders, or a grooved or

pitted outcrop. Both will increase the amount of material required for detection.

As an illustration of the cavity effect, if calcrete with a 4.8% band depth has 83% of the radiance exit with one reflection from a rough region, and 17% of the radiance exits with no reflections from a rough region, a 1% band depth will be observed (Equation 1). This shows the importance of considering effects of roughness at sizes larger than the sample, an effect that is very rarely reproduced in laboratory studies of massive materials, and thus rarely considered in evaluations of detection limits.

Spectra measured by the airborne SEBASS provide another illustration of field vs. laboratory results. SEBASS measured high quality spectra of calcrete from the same area of Mormon Mesa as the calcrete sample that produced the laboratory spectrum shown in Figure 7.<sup>34</sup> Spectra recorded at  $\sim 2 \times 2 \text{ m}^2$  spatial resolution of regions with near 100% coverage by calcrete exhibit an  $11.25 \mu\text{m}$  band depth of  $\sim 1\%$ , convolved to the TES spectral resolution.<sup>34</sup> This is a reduction by a factor of  $\sim 4.8$  relative to the depth predicted based purely on laboratory measurements. An undetermined combination of the cavity effect, reflected downwelling radiance, and mixed pixel effect causes the lowered band contrast relative to the laboratory spectrum. The contribution from reflected downwelling radiance depends on the temperature and water content of the atmosphere, cloud coverage, and the reflectance at the band center of interest. Whatever the cause, the reduced band contrast illustrates the importance of extending spectral studies from the laboratory to the field in order to improve knowledge of effects that are not commonly reproduced in laboratory spectral measurements. It also illustrates that a material detection limit based only on laboratory spectra will likely be optimistically lower (more sensitive) than will actually occur in field measurements. Finally, these hyperspectral measurements dramatically illustrate the importance of stating the material's assumed spectral contrast for any statement of material detection limits.

## 7. Conclusions

We have presented a method to calculate the detection limit for bands recorded in remotely sensed measurements. The band detection limit depends on the instrument SNR, spectral resolution and sampling interval, the desired signal relative to the noise, and the confidence in the instrument calibration and atmospheric compensation. The material detection limit depends on the band detection limit combined with the width and depth of bands exhibited by the material.

The band depth of minerals and rocks varies significantly with properties unrelated to composition, such as the presence of pits that cause a cavity effect (e.g. pits between pebbles, interstices between grains, pits and

grooves in rocks, and vesicles), and volume scattering due to the presence of rough, angular, or very small particles. The cavity effect on a scale larger than the laboratory sample and reflected downwelling radiance also degrade the spectral contrast of materials measured in the field relative to the laboratory. Thus for a quoted detection limit to have meaning, it is not sufficient to state the mineral or rock type, but the material's assumed band depths must also be given. For example, typical studies that utilize TES data give detection limits of ~5–10% for carbonates,<sup>47,48</sup> with the unstated assumptions that the carbonate is well-crystalline, present in large grain sizes, has a smooth surface at all scales, and there is no reflected downwelling radiance. Based on those measurements, it has been concluded that TES has not detected carbonates.<sup>47,48</sup> However, for clarity, it is important to state the assumed band depths and physical properties of the target material used to determine the detection limit, and not just give a detection limit. In addition, the method and specific bands used to calculate the detection limit should be given.

Finally, the detection limit varies with signal, and signal varies with wavelength. Thus the strongest and widest band exhibited by a mineral in the laboratory

may actually not be the most detectable by a given remote sensing instrument. This critical point is still often overlooked. It should be kept in mind when designing an instrument and determining and stating detection limits, and when searching a data base for the signature of a given mineral.

**Acknowledgments.** Thanks to Paul M. Adams (The Aerospace Corporation) for measuring the laboratory spectra and composition information of the samples; John Hackwell and Eric Keim (The Aerospace Corp.) for their unique SEBASS data; Brian Fessler, Scott Lee (Lunar and Planetary Institute, LPI), and Donald Stone (The Aerospace Corp.) for unraveling the TES digitization method; the LPI librarians for their tenacious help in finding and obtaining TES documentation; Raymond Arvidson (Washington U.) and his NASA Planetary Data System group for their exceptional work archiving TES data; Karl Westberg and Stephen Young (The Aerospace Corp.) and three anonymous reviewers whose comments considerably improved the manuscript; and LPI and The Aerospace Corporation for supporting this study, and fundamental studies of applied infrared remote sensing. LPI contribution 1094.

## References and Notes

1. See, for example, D. E. Sabol, J. B. Adams and M. O. Smith, "Quantitative subpixel detection of targets in multispectral images," *J. Geophys. Res.* **97**, 2659-2672, (1992).
2. See, for example, P. E. Johnson, M. O. Smith, and J. B. Adams, "Simple algorithms for remote determination of mineral abundances and particle sizes from reflectance spectra," *J. Geophys. Res.* **97**, 2649-2657, (1992).
3. See, for example, J. B. Adams, M. O. Smith, and A. R. Gillespie, *Imaging spectroscopy: Interpretation based on spectral mixture analysis*, ch.7 in *Remote Geochemical Analysis: Elemental and Mineralogical Composition*, C. Pieters and P. Englert ed., (Cambridge UP, 1993).
4. W. K. Pratt, *Digital Imaging Processing*, ch. 19, (John Wiley, New York, 1978).
5. W. H. Farrand and J. C. Harsanyi, "Discrimination of poorly exposed lithologies in imaging spectrometer data," *J. Geophys. Res.* **100**, 1565-1578, (1995).
6. J. F. Mustard and J. M. Sunshine, "Spectral analysis for Earth science: Investigations using remote sensing data," ch. 5 in *Remote Sensing for the Earth Sciences: Manual of Remote Sensing, 3 ed. Vol. 3*, A. N. Rencz, ed., (Wiley, New York, 1999).
7. G. R. Hunt and L. M. Logan, "Variation of single particle mid-infrared emission spectrum with particle size," *App. Op.* **11**, 142-147, (1972).
8. J. L. Thomson and J. W. Salisbury, "The mid-infrared reflectance of mineral mixtures (7-14  $\mu\text{m}$ )," *Remote Sens. of Environment* **45**, 1-13, (1993).
9. B. Hapke, *Theory of Reflectance and Emittance Spectroscopy*, (Cambridge UP, 1993).
10. J. W. Salisbury and A. Wald, "The role of volume scattering in reducing spectral contrast of reststrahlen bands in spectra of powdered minerals," *Icarus* **96**, 121-128, (1992).
11. R. K. Vincent and F. Thomson, "Spectral composition imaging of silicate rocks," *J. Geophys. Res.* **77**, 2465-2472, (1972).
12. A. R. Gillespie, A. B. Kahle, and R. E. Walker, "Color enhancement of highly correlated images. I. Decorrelation stretch," *Rem. Sens. Environ.* **20**, 209-235, (1986).
13. A. R. Gillespie, "Spectral mixture analysis of multispectral thermal infrared images," *Rem. Sens. Environ.* **42**, 137-145, (1992).
14. H. Shipman and J. B. Adams, "Detectability of minerals on desert alluvial fans using reflectance spectra," *J. Geophys. Res.* **92**, 10,391-10,402, (1987).

15. A. R. Gillespie, "Spectral mixture analysis of multispectral thermal infrared images," *Rem. Sens. Environ.* **42**, 137-145, (1992).
16. T. D. Rubin, "Spectral mapping with imaging spectrometers," *Photogramm. Engineer. & Remote Sens.* **59**, 215-220, (1993).
17. A review of references are given in M. L. Polak, J. L. Hall, and K. C. Herr, "Passive Fourier-transform infrared spectroscopy of chemical plumes: an algorithm for quantitative interpretation and real-time background removal," *Appl. Opt.* **34**, 5406-5412, (1995).
18. A review of references are given in D. F. Flanigan, "A short history of remote sensing of chemical agents," in *Electro-Optical Technology for Remote Chemical Detection and Identification*, M. Fallahi and E. Howden, eds., *Proc. SPIE Vol. 2763*, 2-17, (1996).
19. An application to Mars is given in J. M. McAfee, *Interpretation of the infrared spectra of the Martian atmosphere obtained by the Mariner 6 and 7 Infrared Spectrometers*, Ph.D. thesis, U. California at Berkeley, (1974).
20. P. R. Christensen, D. L. Anderson, S. C. Chase, R. N. Clark, H. H. Kieffer, M. C. Malin, J. C. Pearl, J. Carpenter, N. Bandiera, F. G. Brown, and S. Silverman, "Thermal emission spectrometer experiment: Mars Observer mission," *J. Geophys. Res.* **97**, 7719-7734, (1992).
21. Hanel et al. [1992, p.345] used 7.81  $\mu\text{m}$ . R. A. Hanel, B. J. Conrath, D. E. Jennings, and R. E. Samuelson, *Exploration of the Solar System by Infrared Remote Sensing*, (Cambridge UP, 1992).
22. Kirkland and Herr [2000] use 7.75  $\mu\text{m}$ . L. E. Kirkland and K. C. Herr, "Spectral anomalies in the 11 and 12  $\mu\text{m}$  region from the Mariner Mars 7 Infrared Spectrometer," *J. Geophys. Res.* **105**, 22507-22515, (2000).
23. Smith et al. [2000] use 7.6-7.8  $\mu\text{m}$ . M. D. Smith, J. L. Bandfield, and P. R. Christensen, "Separation of atmospheric and surface spectral features in Mars Global Surveyor Thermal Emission Spectrometer (TES) studies," *J. Geophys. Res.* **105**, 9589-9607, (2000).
24. C. L. Wyatt, *Radiometric System Design*, (Macmillan, New York, 1987), p.145.
25. J. R. Aronson, A. G. Emslie, R. V. Allen, and H. G. McLinden, "Studies of the middle- and far-infrared spectra of mineral surfaces for application in remote compositional mapping of the moon and planets," *J. Geophys. Res.* **72**, 687-703, (1967).
26. C. S. Williams and O. A. Becklund, *Optics: A Short Course for Engineers*, (Krieger, Florida, 1984), pp. 58-63.
27. J. Fraden, *AIP Handbook of Modern Sensors*, (AIP, New York, 1993), p.136.
28. P. R. Griffiths and J. A. de Haseth, *Fourier Transform Infrared Spectrometry*, (John Wiley, New York, 1986).
29. P. R. Christensen, Calibration report for the Thermal Emission Spectrometer (TES) for the Mars Global Surveyor mission, *Jet Propulsion Lab. document D-19020*; microfiche file 741-314, (1998), available through the Jet Propulsion Lab, Pasadena or the Lunar and Planetary Institute, Houston.
30. J. D. Bowman, E. A. Guinness, S. Slavney, R. E. Arvidson, Mars Global Surveyor Thermal Emission Spectrometer Time Sequential Data Record Standard Product, *Planetary Data System archive of TES data*, (1999). The data set is available to all interested researchers through the NASA Planetary Data System Geosciences Node, Washington University, St. Louis.
31. J. A. Hackwell, D. W. Warren, R. P. Bongiovi, S. J. Hansel, T. L. Hayhurst, D. J. Mabry, M. G. Sivjee, and J. W. Skinner, "LWIR/MWIR Imaging Hyperspectral Sensor for Airborne and Ground-Based Remote Sensing," in *Imaging Spectrometry II*, M. Descour, J. Mooney, eds., *Proc. SPIE* **2819**, 102-107, (1996).
32. Thermal Emission Spectrometer (TES) software specification document, *JPL document number 642-441, vol.5*, (1991), available through the Jet Propulsion Laboratory, Pasadena, or the Lunar and Planetary Institute, Houston.
33. A. S. Wexler, "Integrated intensities of absorption bands in infrared spectroscopy," *Applied Spectroscopy Reviews* **1**, 29-98, (1967).
34. L. E. Kirkland, K. C. Herr, E. R. Keim, J. W. Salisbury, J. A. Hackwell, "A Field Study of Thermal Infrared Spectra of Carbonates, with Implications for Studies of Mars," *Lunar Planet. Sci. Conf. XXXI, abs. 1876*, (2000).
35. L. E. Kirkland, K. C. Herr, P. M. Adams, J. W. Salisbury, and A. Treiman, "A Laboratory Study of Weathered Carbonates, with Implications for the Infrared Remote Sensing of Carbonates on Mars," *Lunar Planet. Sci. Conf. XXXI, abs. 1915*, (2000).
36. J. W. Salisbury, A. Wald, and D. M. D'Aria, "Thermal-infrared remote sensing and Kirchhoff's law I. Laboratory measurements," *J. Geophys. Res.* **99**, 11897-11911, (1994).
37. R. N. Clark and T. D. Roush, "Reflectance spectroscopy: Quantitative analysis techniques for remote sensing applications," *J. Geophys. Res.* **89**, 6329-6340, (1984).
38. Paul Adams, The Aerospace Corporation, *pers. comm.*, (2000).

39. F. A. Kruse, "Use of Airborne Imaging Spectrometer data to map minerals associated with hydrothermally altered rocks in the northern Grapevine Mountains, Nevada, and California," *Remote Sens. Env.* **24**, 31-51, (1988).
40. J. D. Ingle and S. T. Crouch, *Spectrochemical Analysis*, (Prentice Hall, Englewood Cliffs, New Jersey, 1988), pp. 172-174.
41. J. R. Schott, *Remote Sensing: The Image Chain Approach*, (Oxford Press, New York, 1997), pp.191-231.
42. M. D. Smith, J. L. Bandfield, and P. R. Christensen, Separation of atmospheric and surface spectral features in Mars Global Surveyor Thermal Emission Spectrometer (TES) studies, *J. Geophys. Res.* **105**, 9589-9607, (2000).
43. R. A. Hanel, B. J. Conrath, D. E. Jennings, and R. E. Samuelson, *Exploration of the Solar System by Infrared Remote Sensing*, (Cambridge UP, 1992), pp. 256-274.
44. R. Beer, *Remote Sensing by Fourier Transform Spectrometry*, Chemical Analysis Volume 120, (John Wiley, New York, 1992), pp.55-100.
45. J. R. Schott, *Remote Sensing: The Image Chain Approach*, (Oxford Press, New York, 1997), pp.172-180.
46. J. W. Salisbury and D. M. D'Aria, Emissivity of terrestrial materials in the 8-14  $\mu\text{m}$  window, *Remote Sens. Environ.* **42**, 83-106, (1992).
47. See, for example, P. R. Christensen, D. L. Anderson, S. C. Chase, R. T. Clancy, R. N. Clark, B. J. Conrath, H. H. Kieffer, R. O. Kuzmin, M. C. Malin, J. C. Pearl, T. L. Roush, and M. D. Smith, Results from the Mars Global Surveyor Thermal Emission Spectrometer, *Science* **279**, 1692-1698, (1998).
48. See, for example, P. R. Christensen, J. L. Bandfield, M. D. Smith, V. E. Hamilton, R. N. Clark, Identification of a basaltic component on the Martian surface from Thermal Emission Spectrometer data, *J. Geophys. Res.* **105**, 9609-9621, (2000).